applied sciences

MDPI

Article

Two-Step Infrasound Source Localization Method Integrating Spherical-Coordinate Ray Tracing

Hao Yin, Fan Yang and Xinliang Pang *

State Key Laboratory of Chemistry for NBC Hazards Protection, Beijing 102205, China; yinhao1207@163.com (H.Y.); yangfan3132021@126.com (F.Y.)
* Correspondence: pangxinliang@sklnbcpc.cn

Featured Application

The proposed method can support rapid and high-accuracy localization of regional-to-global infrasound events, including artificial explosions, nuclear-test monitoring scenarios, volcanic eruptions, and large-scale atmospheric acoustic events.

Abstract

Infrasound waves attenuate weakly in the atmosphere and can propagate over regional, teleseismic, and global distances, which makes them valuable for monitoring artificial explosions, volcanic eruptions, earthquakes, and nuclear test-related events. Conventional infrasound localization based on the intersection of array back azimuths are computationally efficient, but it often approximates propagation paths as straight geometric rays and therefore cannot fully represent wind fields, temperature gradients, atmospheric waveguides, or Earth curvature. To address this limitation, this paper presents a two-step localization method that couples geometric preliminary localization with local travel-time residual optimization constrained by spherical-coordinate ray tracing. First, multi-station arrival azimuths are intersected, and k-means clustering with least-squares estimation is used to obtain a robust initial source position. Second, a local grid is constructed around the initial solution; for each candidate source, theoretical travel times to the recording stations are calculated using a ray-tracing model for a moving, inhomogeneous atmosphere in spherical coordinates. The final source location is selected by minimizing multi-station travel-time residuals. The method is tested using three representative events: the 2018 Ingolstadt refinery explosion, the 2019 Stromboli eruption, and the 2022 Hunga eruption. The final localization errors are 13.23 km, 5.93 km, and 6.98 km, respectively, corresponding to accuracy improvements of more than 84% relative to conventional geometric localization. The results show that incorporating atmospheric propagation constraints and local residual optimization can substantially reduce systematic bias while maintaining computational efficiency.

Keywords: infrasound localization; spherical-coordinate ray tracing; travel-time residual optimization; wide-area monitoring

Check for updates

Received: 18 August 2026
Revised: 18 October 2026
Accepted: 21 October 2026
Published: 24 October 2026

Copyright: © 2026 by the authors. Licensee MDPI, Basel, Switzerland. This article is an open access article distributed under the terms and conditions of the Creative Commons Attribution (CC BY) license.

1. Introduction

Infrasound refers to elastic waves with frequencies below 20 Hz. Its atmospheric attenuation decreases markedly with decreasing frequency, and it can propagate over extremely long distances through atmospheric waveguides formed by wind and temperature gradients. Owing to these unique physical characteristics, infrasound technology has been widely used for the remote monitoring of anthropogenic events and natural hazards,

including nuclear tests, chemical explosions, volcanic eruptions, and earthquakes. To promote the implementation and entry into force of the Comprehensive Nuclear-Test-Ban Treaty, the Comprehensive Nuclear-Test-Ban Treaty Organization (CTBTO) has established an International Monitoring System (IMS) consisting of 53 certified infrasound arrays worldwide, with a planned total of 60 arrays, enabling global detection and localization of infrasonic events.

Conventional infrasound localization methods are mainly based on array-processing techniques. These methods estimate the direction of arrival of infrasonic signals using generalized cross-correlation (GCC)-based time-delay estimation [1–5], the progressive multi-channel correlation method (PMCC) [6–8], beamforming [9–16], or high-resolution spectral estimation [17–21], and then determine the source location through multi-station azimuthal intersection. Such approaches are simple to implement, computationally efficient, and suitable for engineering applications. Their localization performance, however, depends critically on the accuracy of back-azimuth estimation. During long-range propagation, infrasonic signals are strongly affected by atmospheric wind fields, temperature gradients, and other propagation effects. As a result, the observed arrival direction may deviate significantly from the true source direction. In severe cases, the back-azimuth error can reach several degrees, leading to localization errors of hundreds of kilometers for large-scale events.

To mitigate the influence of propagation effects on localization accuracy, physical propagation models have gradually been incorporated into infrasonic source localization, leading to methods based on atmospheric acoustic propagation, such as ray tracing, parabolic equation modeling, and reverse time migration. Ray tracing, which is based on geometrical acoustics, calculates acoustic ray trajectories in the atmosphere to obtain propagation parameters such as azimuth and energy, thereby correcting back-azimuth deviations [22,23]. Typical applications include the use of atmospheric models such as NRL-G2S and ECMWF, combined with three-dimensional ray-tracing programs, to calculate back-azimuth deviations for Geiger-method localization corrections [24–27], which can significantly reduce localization errors. Reverse time migration (RTM), in contrast, is a time-domain back-propagation technique that reconstructs the source location by propagating received signals backward along modeled propagation paths and stacking waveform-envelope amplitudes. RTM does not rely on a specific array geometry and can handle complex wavefields, achieving localization errors of less than 20 m within a range of 15 km [28]. However, this method requires an accurate velocity model and substantial computational resources, which limits its applicability to long-range monitoring scenarios.

Because the stochastic and time-varying state of the atmosphere introduces significant uncertainty into infrasound propagation, Bayesian infrasonic source localization (BISL) methods have developed rapidly over the past decade [25,29–33]. BISL treats source location, event origin time, and propagation velocity as random variables and constructs a likelihood function by jointly using back azimuths and arrival times. By incorporating prior distributions of atmospheric propagation velocity and probabilistic likelihood functions, BISL can provide both source-location estimates and associated confidence regions. Its main advantage lies in its ability to integrate propagation uncertainty, measurement errors, and model errors. Nevertheless, its global probabilistic search strategy still suffers from high computational cost and slow convergence, and it has not yet been widely applied to global-scale infrasonic events.

Overall, existing infrasonic source localization methods have their respective advantages, but a significant trade-off remains between computational efficiency and physical accuracy. Traditional array-based localization methods are fast and straightforward, but they neglect atmospheric propagation effects, so back-azimuth deviations may lead to

large localization errors. Propagation-based inversion methods can accurately describe the underlying physical processes, but their high computational cost restricts their application in large-scale monitoring scenarios. Bayesian probabilistic methods have favorable statistical properties, but they are sensitive to parameter settings, prior information, and search strategies.

To address these limitations, this study proposes a two-step infrasonic source localization method based on ray tracing in a spherical-coordinate, inhomogeneous medium. The proposed method first estimates the direction of arrival using infrasound arrays and obtains an initial source location through multi-station azimuthal intersection. It then refines the source location through local fine-grid search and ray-tracing-based travel-time residual optimization, thereby balancing real-time performance and physical accuracy in wide-area monitoring scenarios. The main contributions of this study are as follows: (1) a complete set of Hamiltonian canonical equations for ray tracing in a moving medium under a spherical-coordinate system is derived, together with explicit geometric correction terms, ensuring the self-consistency of global-scale propagation modeling under spherical geometry; (2) a two-stage localization framework, consisting of rapid preliminary localization and grid-based optimization, is proposed to confine the computationally expensive propagation modeling to a small neighborhood, thereby avoiding the large computational burden of global propagation calculations while maintaining localization accuracy; and (3) the cross-scale applicability and superior performance of the proposed method are systematically validated across real-world medium-range, long-range, and global-scale events, achieving a localization accuracy improvement of over 764% compared with conventional methods and constraining the absolute localization error to within 7 km.

2. Materials and Methods

2.1. Ray-Tracing Model in a Spherical-Coordinate Inhomogeneous Moving Medium

During long-range infrasound propagation, the adiabatic sound speed of the atmospheric medium and the ambient wind field exhibit significant spatial heterogeneity. Meanwhile, the characteristic spatial scale of atmospheric variations is much larger than the infrasonic wavelength, satisfying the approximation conditions of geometrical acoustics. Based on geometrical acoustics, this study establishes an infrasonic ray-tracing model in an inhomogeneous moving medium and further extends it to a spherical-coordinate system to meet the requirements of global-scale propagation modeling.

2.1.1. Ray Tracing in a Moving Inhomogeneous Atmosphere

When the spatial variation scale of atmospheric parameters is much larger than the acoustic wavelength, geometrical acoustics provides an efficient approximation for infrasound propagation. Let $\vec{x} = (x, y, z)$ denote the spatial position of the ray, $c(\vec{x})$ denote the spatially varying adiabatic sound speed, $\vec{v}(\vec{x})$ denote the background ambient wind velocity, c_{src} denote the sound speed at the source location, and $\vec{\psi}$ denote the eikonal vector normal to the acoustic wavefront. In a moving medium, acoustic-wave propagation is governed by the eikonal equation [34]:

$$\psi^2 = \frac{c_{\mathrm{src}}^2}{c^2(\vec{x})}\left(1 - \frac{\vec{\psi}\cdot\vec{v}(\vec{x})}{c_{\mathrm{src}}}\right)^2, \tag{1}$$

The Hamiltonian is defined as

$$\left(\vec{x}, \vec{\psi}\right) = \frac{1}{2}\left[\psi^2 - \frac{c_{\mathrm{src}}^2}{c^2(\vec{x})}\left(1 - \frac{\vec{\psi}\cdot\vec{v}(\vec{x})}{c_{\mathrm{src}}}\right)^2\right], \tag{2}$$

and the actual ray path satisfies the constraint $H\left(\vec{x}, \vec{\psi}\right) = 0$.

Introducing the parameter ξ, the canonical ray equations can be expressed as

$$\frac{\partial \vec{x}}{\partial \xi} = \frac{\partial H}{\partial \vec{\psi}}, \frac{\partial \vec{\psi}}{\partial \xi} = -\frac{\partial H}{\partial \vec{x}}, \tag{3}$$

To give the numerical integration a clear physical meaning, the physical ray arclength s is further adopted as the independent variable. The ray-path equation in Cartesian coordinates is then obtained as

$$\frac{\partial \vec{x}}{\partial s} = \frac{\vec{c}_g}{c_g}, \tag{4}$$

where $\vec{c}_g$ is the group-velocity vector, defined as $\vec{c}_g = c\frac{\vec{\psi}}{\psi} + \vec{v}$, and its magnitude is $c_g = \left|\vec{c}_g\right|$.

For the j-th Cartesian component of the eikonal vector, one obtains

$$\frac{\partial \psi_j}{\partial s} = -\frac{1}{c_g}\left(\psi \frac{\partial c}{\partial x_j} + \vec{\psi} \cdot \frac{\partial \vec{v}}{\partial x_j}\right), j = 1, 2, 3, \tag{5}$$

Equation (4) describes the variation of the ray position with arclength, whereas Equation (5) describes the variation of the ray direction caused by atmospheric sound-speed gradients and wind-velocity gradients. Specifically, sound-speed gradients induce acoustic refraction, while the wind field and wind shear jointly influence the ray path through the group velocity and the eikonal vector.

2.1.2. Ray-Tracing Equations in Spherical Coordinates

For propagation over thousands of kilometers or even on a global scale, a spherical-coordinate system must be adopted to accurately describe the curvature of the Earth. The spherical coordinates are defined as (r,θ,ϕ), where r is the radial distance from the center of the Earth, θ is latitude, and ϕ is longitude. The height of the ray relative to the Earth's surface can be expressed as

$$z = r - r_e,$$

where r_e is the reference radius of the Earth.

It should be noted that latitude is used here; therefore, the scale factors in the spherical-coordinate system are

$$h_r = 1, h_\theta = r, h_\phi = r\cos\theta, \tag{6}$$

and the corresponding geometric scaling coefficients are

$$G_r = 1, G_\theta = \frac{1}{r}, G_\phi = \frac{1}{r\cos\theta}, \tag{7}$$

The three spherical-coordinate components of the group velocity are given by

$$c_{g,r} = c\frac{\psi_r}{\psi} + v_r, \tag{8a}$$

$$c_{g,\theta} = c\frac{\psi_\theta}{\psi} + v_\theta, \tag{8b}$$

$$c_{g,\phi} = c\frac{\psi_\phi}{\psi} + v_\phi, \tag{8c}$$

The spatial position equations in the spherical-coordinate system are obtained as

$$\frac{\partial r}{\partial s} = \frac{c_{g,r}}{c_g}, \tag{9a}$$

$$\frac{\partial \theta}{\partial s} = \frac{1}{r}\frac{c_{g,\theta}}{c_g}, \tag{9b}$$

$$\frac{\partial \phi}{\partial s} = \frac{1}{r\cos\theta}\frac{c_{g,\phi}}{c_g}, \tag{9c}$$

According to the spatial variation relationships of the basis vectors in the spherical-coordinate system, the three geometric correction terms can be explicitly written as

$$T_r = \frac{1}{r}\left(\psi_\theta c_{g,\theta} + \psi_\phi c_{g,\theta}\right), \tag{10a}$$

$$T_\theta = (\psi_r v_\theta - \psi_\theta v_r) - (\psi_r c_{g,\theta} + \psi_\phi c_{g,\phi}\tan\theta), \tag{10b}$$

$$T_\theta = (\psi_r v_\theta - \psi_\theta v_r) - (\psi_r c_{g,\theta} + \psi_\phi c_{g,\phi}\tan\theta) - c_{g,\phi}(\psi_r\cos\theta + \psi_\theta\sin\theta), \tag{10c}$$

Therefore, the evolution equations for the components of the eikonal vector in the spherical-coordinate system are

$$\frac{\partial \psi_r}{\partial s} = -\frac{1}{c_g}\left(\psi\frac{\partial c}{\partial r} + \sum\nolimits_k \psi_k \frac{\partial v_k}{\partial r}\right) + T_r, \tag{11a}$$

$$\frac{\partial \psi_\theta}{\partial s} = -\frac{1}{rc_g}\left(\psi\frac{\partial c}{\partial \theta} + \sum\nolimits_k \psi_k \frac{\partial v_k}{\partial \theta}\right) + T_\theta, \tag{11b}$$

$$\frac{\partial \psi_\phi}{\partial s} = -\frac{1}{r\cos\theta c_g}\left(\psi\frac{\partial c}{\partial \phi} + \sum\nolimits_k \psi_k \frac{\partial v_k}{\partial \phi}\right) + T_\phi, \tag{11c}$$

Equations (9) and (11) together constitute a six-dimensional ray-tracing system for an inhomogeneous moving atmosphere in spherical coordinates. Unlike a simple treatment in which Cartesian coordinates are merely replaced by latitude and longitude, this equation system simultaneously accounts for the scale factors of the spherical-coordinate system, the curvature of the Earth's surface and atmosphere, the spatial variation of the local spherical basis vectors, refraction caused by spatial gradients of sound speed, and advection and ray bending induced by background wind and wind shear.

Ray tracing also requires the source location and the initial emission direction to be specified. Let the source location be (r_0,θ_0,ϕ_0), and let the initial elevation angle and azimuth angle of the ray be α and β, respectively. If the azimuth is measured clockwise from geographic north, the unit direction vector in the local coordinate system can be written as

$$\vec{n}_0 = \sin\alpha\hat{e}_r + \cos\alpha\cos\beta\hat{e}_\theta + \cos\alpha\sin\beta\hat{e}_\phi, \tag{12}$$

Let the initial eikonal vector be

$$\vec{\psi}_0 = \lambda\vec{n}_0,$$

At the source location $c(\vec{x}_0) = c_{src}$. Substituting this relation into the eikonal equation, Equation (1), and taking the positive solution corresponding to outward energy propagation gives

$$\lambda = \frac{1}{1 + \vec{n}_0\cdot\vec{v}_0/c_{src}} \tag{13}$$

Thus,

$$\vec{\psi}_0 = \frac{\vec{n}_0}{1 + \vec{n}_0\cdot\vec{v}_0/c_{src}}, \tag{14}$$

If the wind speed near the source is much smaller than the sound speed, the following approximation holds:

$$\vec{\psi}_0 \approx \vec{n}_0, \tag{15}$$

Equation (15) ensures that the initial eikonal vector simultaneously satisfies the prescribed emission direction and the eikonal constraint for a moving medium.

2.1.3. Travel-Time Calculation

The group velocity represents the actual propagation velocity of acoustic energy along the ray path. Therefore,

$$\frac{d\tau}{ds} = \frac{1}{c_g}, \tag{16}$$

The total travel time from the source position to the receiver position along the ray path is given by

$$\tau = \int_{s_0}^{s_1} \frac{ds}{c_g(s)} = \int_{s_0}^{s_1} \frac{ds}{\left| c\frac{\vec{\psi}}{\psi} + \vec{v} \right|}, \tag{17}$$

In the spherical-coordinate system, the arc-length element satisfies

$$ds^2 = dr^2 + r^2 d\theta^2 + r^2(\cos\theta)^2 d\phi^2, \tag{18}$$

The form of the travel-time integral itself is independent of the coordinate system. However, the ray path, group velocity, and arclength element must all be calculated using the spherical-coordinate ray equations.

2.2. Two-Step Infrasound Localization Method Integrating Atmospheric Acoustic Propagation

This paper proposes a two-step localization strategy consisting of conventional geometric preliminary localization and local grid-search optimization. The overall workflow is shown in Figure 1. The first step is conventional geometric localization. First, arrival parameters, including arrival time, back azimuth, and propagation velocity, are extracted from infrasound data recorded by multiple stations or arrays. Then, based on the station back azimuths and geographic coordinates, bearing lines are constructed and spatially intersected. Finally, according to the number of intersection points and their spatial consistency, an appropriate initial-location estimation scheme is selected to obtain the preliminary source location. The second step is local grid-search optimization. Using the preliminary source location, event time, and station locations as input parameters, a propagation environment is constructed, including empirical atmospheric models, ERA5 reanalysis data, and empirical climatological models above 80 km altitude. These atmospheric data are used to generate propagation profiles containing horizontal wind, temperature, density, and pressure. Subsequently, spherical-coordinate three-dimensional infrasound ray tracing is used to calculate the theoretical propagation time from each candidate source point to each station. Finally, the final source location is determined by minimizing the difference between the observed and theoretical travel times. This workflow combines the computational efficiency of geometric localization with the physical constraints provided by propagation-model correction. It can adapt to different observation conditions, including variations in station number and event distance, and improves infrasound source localization accuracy while reducing the computational cost of global search.

2.2.1. Initial Position Estimation Based on Infrasound Arrays

To address the limitations of conventional short-time energy-change detection methods, in which the threshold is usually determined empirically, and the detection results are easily affected by background noise and array-element response differences, this study improves the arrival-time picking and azimuth-estimation procedures while retaining the overall technical route of short-time energy-change detection—inter-element time-difference estimation—array geometry-based direction-of-arrival estimation. The main improvements include normalization of short-time energy features, adaptive threshold determination, constraint of candidate change intervals, and refined arrival-time picking. These procedures effectively reduce the influence of fixed thresholds on detection results and improve the

stability and reproducibility of the algorithm under different signal-to-noise ratios, station responses, and complex background-noise conditions.

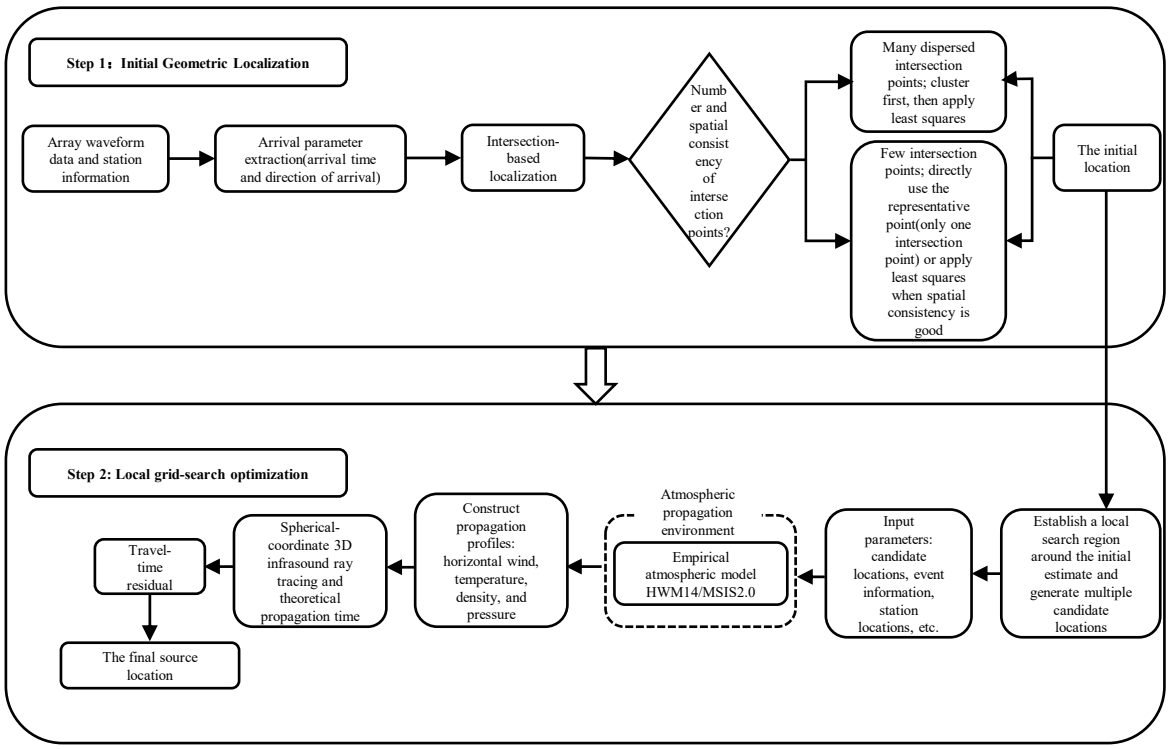


Figure 1. Schematic workflow of the two-step infrasound localization method integrating atmospheric acoustic propagation.

Let $x_i(n)$ denote the signal received by the i-th element of an array. The signals recorded by all array elements are first preprocessed, including demeaning, detrending, band-pass filtering, and amplitude normalization, when necessary, in order to suppress the influence of low-frequency drift, random noise, and array-element gain differences on subsequent energy calculations. On this basis, the short-time energy of each array element is calculated using a sliding time window:

$$E_i(n) = \sum_{m=0}^{L-1} w(m) x_i^2(n-m), \tag{19}$$

where L is the length of the short-time window, and $w(m)$ is the window function, which is generally selected as a rectangular window. Unlike methods that directly apply threshold discrimination to the raw short-time energy, this study further constructs a normalized energy-change feature to characterize the deviation of the current short-time energy from the local background-noise level. Specifically, a robust standardization form based on the median and median absolute deviation can be adopted:

$$C_i(n) = \frac{\log\left(E_i(n) + \varepsilon\right) - \text{median}[\log(E_i)]}{1.4826\text{MAD}[\log(E_i)] + \varepsilon}, \tag{20}$$

Here, ε is a small positive constant used to avoid division by zero. Both the median and MAD are estimated within the pre-event background window or a sliding background window. This treatment maps the energy variations of different array elements onto a unified relative change-intensity scale, thereby avoiding the incomparability of energy amplitudes caused by differences in element sensitivity, propagation-path attenuation, or local noise conditions.

During the change-detection stage, this study no longer adopts a manually fixed threshold. Instead, the detection threshold is adaptively determined according to the statistical characteristics of the background noise. Specifically, the empirical distribution of the normalized change feature $C_i(n)$ is estimated within a background window where no valid signal arrival is present, and the quantile threshold is selected according to a prescribed false-alarm probability α:

$$h_i = Q_{1-\alpha} C_i(k), k \in \Omega_i, \tag{21}$$

where Ω_i denotes the background-noise sample set corresponding to the i-th array element, and $Q_{1-\alpha}$ is its $(1-\alpha)$-quantile. In this way, the threshold can adaptively vary with the local noise level of each array element, and the detection procedure obtains a clear statistical meaning. Compared with empirical thresholds, this method can maintain relatively stable false-alarm control under different noise environments, thereby improving the objectivity and reproducibility of change detection.

It should be noted that the adaptive threshold in the proposed method is mainly used to determine candidate change intervals, rather than serving directly as the final arrival-time criterion. For the i-th array element, when the normalized change feature $C_i(n)$ exceeds the adaptive threshold h_i, this time interval is only considered to potentially contain a valid signal arrival, and a candidate search window W_i is constructed accordingly. Within the candidate window, the precise arrival time is further determined using the energy-change rate, local maximum, or statistical change criterion. This strategy avoids the high sensitivity of the conventional "first threshold crossing" method to the selected threshold, allowing arrival-time estimation to rely more on the local structural characteristics of the signal rather than on a single threshold position.

To further improve the accuracy of arrival-time picking, the point with the maximum energy variation within the candidate change interval is taken as the initial arrival-time estimate:

$$\hat{t}_i^{(0)} = \underset{n \in W_i}{\operatorname{argmax}} [C_i(n) - C_i(n-1)], \tag{22}$$

A refined search is then performed in its neighborhood using the Akaike information criterion (AIC). The AIC arrival-time picking method regards the signal arrival time as the boundary at which the statistical characteristics before and after the candidate point change. Its objective function can be expressed as

$$k \log \sigma_{i,1}^2(k) + (N-k-1) \log \sigma_{i,2}^2(k), \tag{23}$$

where $\sigma_{i,1}^2(k)$ and $\sigma_{i,2}^2(k)$ denote the variances of the two signal segments before and after the candidate point k, respectively. The final arrival-time estimate is obtained as

$$\hat{t}_i = \underset{k \in \acute{W}_i}{\operatorname{argmin}} \mathrm{AIC}_i(k), \tag{24}$$

where W_i' is the local search window around the initial change point. This procedure preserves the advantages of short-time energy-change detection while correcting the final arrival time from the energy-peak position to the statistically meaningful onset position, thereby reducing the influence of energy-envelope delay on time-difference estimation.

After obtaining the arrival-time estimates $\hat{t}_i$ for each array element, the arrival-time difference between an element pair can be calculated as

$$\tau_{ij} = \hat{t}_i - \hat{t}_j, \tag{25}$$

Considering that different array elements may have different signal-to-noise ratios and change sharpness, this study further assigns an uncertainty measure to each arrival-time estimate. This uncertainty can be estimated from the sharpness of the change peak

within the candidate window, the local signal-to-noise ratio, the curvature of the AIC curve, or resampling methods. Accordingly, the uncertainty of the time difference between an element pair can be expressed as

$$\sigma_{\tau_{ij}}^2 = \sigma_{t_i}^2 + \sigma_{t_j}^2, \tag{26}$$

In azimuth inversion, the contribution of each element pair should be consistent with the reliability of its time-difference estimate. Therefore, the following weight can be adopted:

$$w_{ij} = \frac{1}{\sigma_{\tau_{ij}}^2 + \varepsilon}, \tag{27}$$

This weighting strategy reduces the influence of weak-change elements, low-SNR elements, or potentially mispicked elements on the final azimuth-estimation result.

Combined with the array geometry, let $\mathbf{b}_{ij}$ denote the baseline vector between array elements i and j, $\mathbf{u}(\theta)$ denote the unit vector of the arrival direction, and v denote the propagation velocity. The theoretical time difference can then be expressed as

$$\tau_{ij}(\theta) = \frac{\mathbf{b}_{ij}^T \mathbf{u}(\theta)}{v}, \tag{28}$$

For a two-dimensional planar direction-finding problem,

$$\mathbf{u}(\theta) = [\cos\theta, \sin\theta]^{\mathrm{T}}, \tag{29}$$

Thus, the direction-of-arrival azimuth can be estimated using a weighted nonlinear least-squares method:

$$\hat{\theta} = arg\min_{\theta} \sum_{i<j} w_{ij} \rho \left[\hat{\tau}_{ij} - \frac{\mathbf{b}_{ij}^T \mathbf{u}(\theta)}{v} \right], \tag{30}$$

This method can maintain relatively stable azimuth-estimation performance even when arrival-time picking errors exist for some array elements.

After the direction-of-arrival azimuths are obtained from two or more stations, spatial observation rays can be constructed based on the station locations and corresponding azimuths. Candidate intersection points of the target location are then obtained through pairwise intersections of observation rays from different stations. Due to azimuth-estimation errors, differences in station geometry, and local anomalous observations, the candidate intersection points usually do not converge to a single location but instead exhibit a certain degree of spatial dispersion. Therefore, directly fitting the source location using all intersection points can be easily affected by outliers or unfavorable geometric intersections, thereby reducing the stability of the initial localization result. To address this issue, this study introduces an initial localization method that combines clustering-based screening with least-squares estimation based on the spatial intersection results [35], thereby improving the robustness and reliability of the initial solution.

2.2.2. Travel-Time Residual Optimization Incorporating Atmospheric Propagation

After obtaining the initial source position from multi-station azimuth intersection, this study further constructs a local search region centered on the initial position. The target location is then refined by matching the residuals between ray-tracing-based forward-modeled travel times and station-observed travel times.

This study aims to estimate signal travel times by modeling infrasound propagation under reasonable atmospheric conditions. The method first generates theoretical travel times corresponding to candidate source points and then compares them with the observed travel times. The candidate source point whose theoretical travel times are closest to the observed values is selected as the final source location. Once the candidate source points,

station locations, event time, and other basic parameters are defined, the proposed method automatically calculates source-to-station propagation times by modeling infrasound propagation using three-dimensional ray tracing and by using a set of empirical atmospheric descriptions obtained from the combination of the Horizontal Wind model 2014 (HWM14) and the Mass Spectrometer and Incoherent Scatter Radar model, NRLMSIS 2.0.

The original climatology refers to the default atmospheric model obtained by combining HWM14 and NRLMSIS 2.0. For each source-to-station direction and event time, horizontal winds, namely zonal and meridional winds, temperature, density, and pressure are sampled every 50 km. For altitude layers from 0 to 170 km with a vertical interval of 0.5 km, each parameter is averaged along the source-to-station direction to obtain an estimated value at each altitude. The resulting model is a layered and range-independent atmosphere that represents the atmospheric characteristics along each ray-propagation direction. It is stored as a table, namely a one-dimensional profile, and used by the ray-tracing algorithm to model infrasound propagation in a three-dimensional spherical layered atmosphere (see Figure 2). For the subsequent atmospheric-model types, the same discretization procedure is adopted. Although the range-independent atmosphere is a strong assumption, it provides a reasonable first-order approximation and reduces the computational cost of three-dimensional ray-tracing propagation. Since real observational data are used to evaluate the effectiveness of the method, future work should consider comparison with more realistic but computationally more expensive models, such as range-dependent ray propagation.

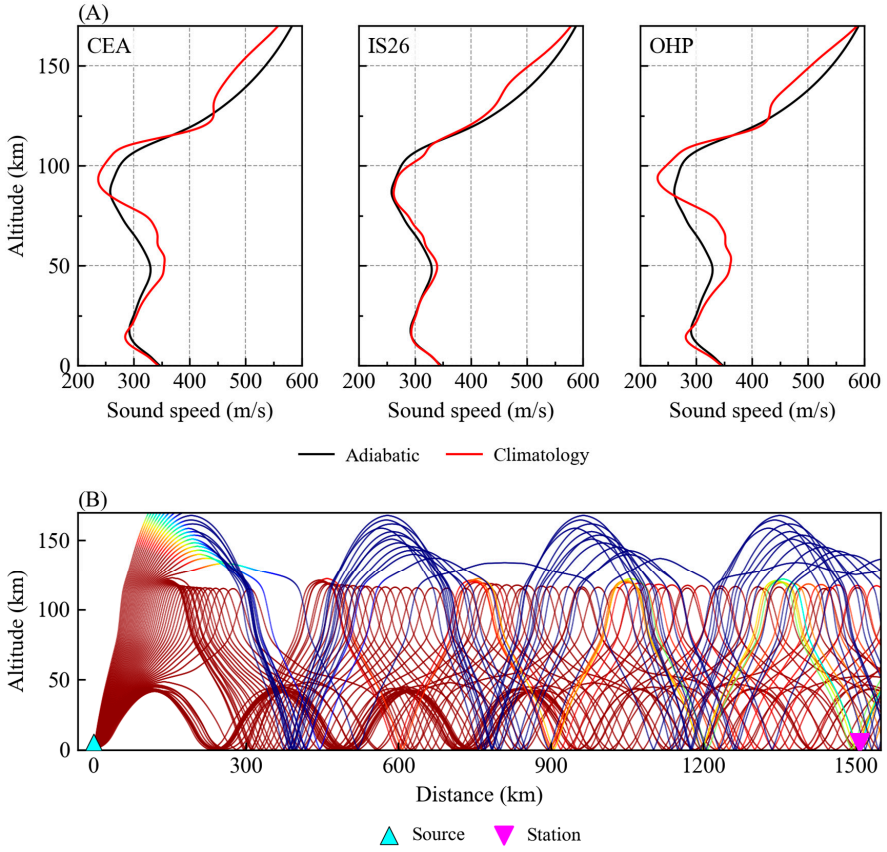


Figure 2. Atmospheric sound-speed profiles and spherical-coordinate ray-tracing results for infrasound propagation: the Stromboli volcanic eruption as an example. (**A**) Adiabatic sound-speed profiles (black) and climatological effective sound-speed profiles (red) along the propagation paths from Stromboli volcano to CEA, IS26, and OHP. (**B**) Ray trajectories simulated in the spherical-coordinate atmosphere, showing the propagation path from the source, Stromboli volcano, to station CEA. The cyan triangle denotes the source, and the magenta triangle denotes the receiving station.

Considering that the uncertainty of the initial source position is mainly affected by azimuth-estimation errors, station geometry, and the spatial dispersion of intersection points, the search range should not be assigned a fixed value arbitrarily. Instead, it should be determined according to the initial localization error. In general, the search range can be set to one to three times the initial localization error.

During grid construction, the search resolution should also be adaptively determined according to the required localization accuracy and computational complexity. In the first two validation cases, the search region is set to ±0.5°, with a horizontal resolution of 0.2°. In the final global-scale volcanic-eruption case, the search region is set to ±1°, with a horizontal resolution of 0.5°. A total of M candidate grid points $\left\{\left(x_j, y_j\right)\right\}_{j=1}^{M}$ are generated.

For each candidate grid point (x_j, y_j), the point is regarded as a virtual source location. According to the spherical-coordinate ray-tracing model described in Section 2.1.3, the theoretical propagation travel time from this candidate source to the k-th station, denoted as $t_{j,k}^{\text{theo}}$, is calculated.

The multi-station travel-time residual sum of squares for the j-th grid point is defined as

$$J(j) = \sqrt{\frac{1}{K}\sum_{k=1}^{K}\left(t_{j,k}^{theo} - t_k^{obs}\right)^2}, \tag{31}$$

The final localization result is the candidate grid point that minimizes the residual objective function:

$$\hat{x} = \text{argmin}_j J(j) \tag{32}$$

3. Results and Discussion

To verify the effectiveness and general applicability of the proposed method, three representative infrasonic events were selected for evaluation. These three cases differ in network geometry, number of stations, terrain conditions, and propagation distance. They are the two-station Ingolstadt refinery explosion, the three-station long-range Stromboli volcanic eruption, and the global-network Hunga volcanic eruption.

3.1. Data

3.1.1. Ingolstadt, Germany, Explosion of 1 September 2018

At 03:11:45 UTC on 1 September 2018, a strong explosion occurred at a refinery in Vosburg, near Ingolstadt, Germany. The source location was 48.766° N, 11.600° E. The event was caused by an oil tank leak and generated prominent seismic and atmospheric acoustic waves, which were recorded by multiple seismic stations and infrasound sensor arrays in Central and Eastern Europe. It is therefore a regional infrasonic event with a well-constrained origin time and source location.

In this study, observations from two infrasound arrays, IGADE and PSZI, were used as the data basis for localization analysis. As shown in Figure 3, IGADE is located northwest of Ingolstadt, with station coordinates of 53.258° N, 8.690° E, approximately 540.2 km from the explosion source. PSZI is located in Hungary, east of Ingolstadt, with station coordinates of 47.918° N, 19.894° E, approximately 622.2 km from the source. Waveform data from these two stations were obtained, and Figure 4 shows the signal waveforms recorded by one element of each array. As shown in the figure, the signal duration at IGADE is relatively long, approximately 3 min, whereas PSZI recorded a clearer infrasonic arrival lasting approximately 1 min.

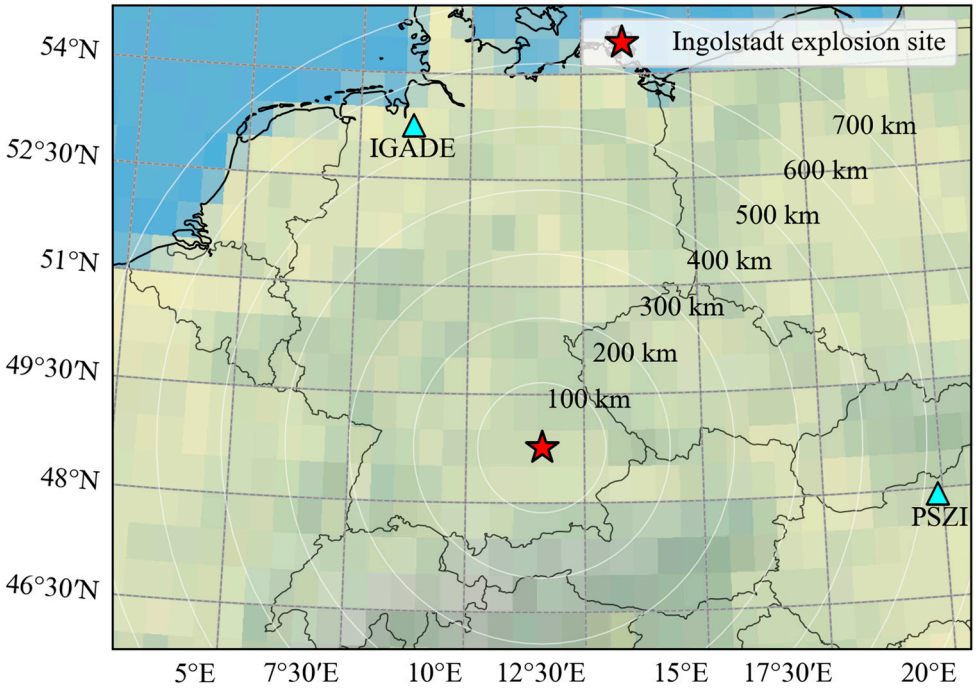


Figure 3. Location map of the Ingolstadt explosion and the infrasound stations IGADE and PSZI.

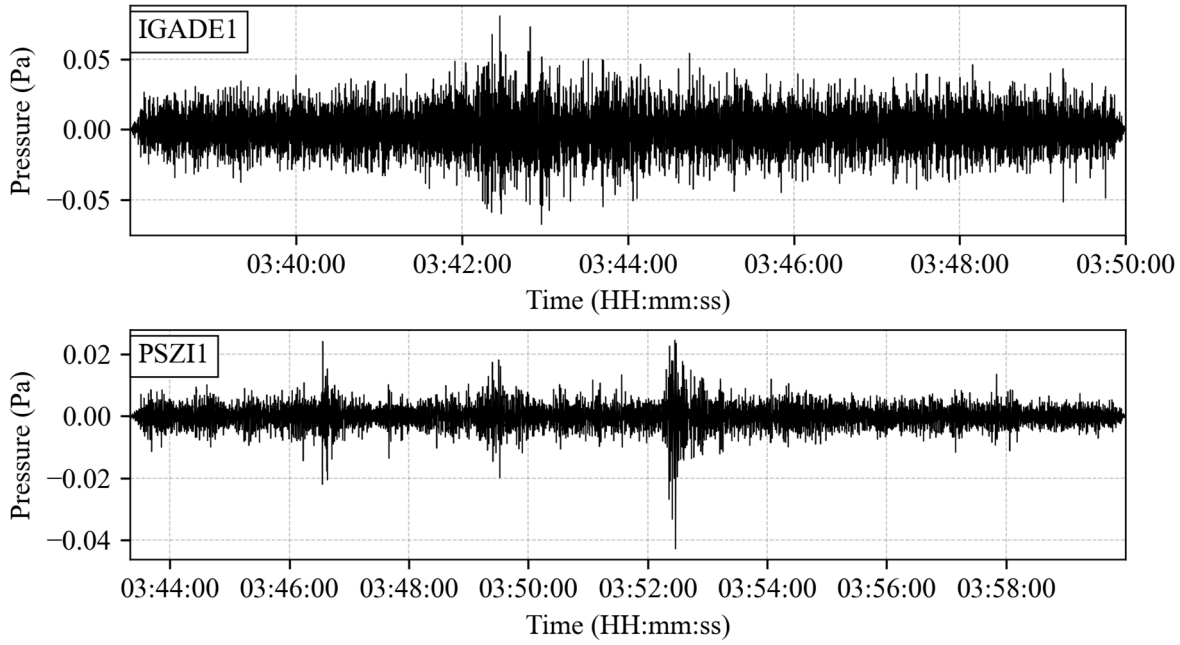


Figure 4. Infrasound waveforms recorded by the IGADE and PSZI arrays after 1–5 Hz band-pass filtering.

3.1.2. The 3 July 2019 Paroxysmal Stromboli Eruptions

At 14:45:42 UTC on 3 July 2019, a strong paroxysmal eruption occurred at Stromboli volcano (38.789° N, 15.213° E), located in the Aeolian Islands north of Sicily, Italy. This eruption consisted of several intense explosions from multiple summit vents separated by several seconds. The event was clearly recorded by the near-field monitoring network on the island and by several far-field infrasound arrays in the Euro-Mediterranean region. It is therefore a volcanic infrasonic event with a well-constrained source location and origin time.

In this study, data from three infrasound stations were obtained: the national infrasound arrays OHP and CEA, and the International Monitoring System infrasound station

I26DE, as shown in Figure 5. The corresponding waveforms are shown in Figure 6. The peak-to-peak sound pressure amplitudes were 6.65 Pa, 0.30 Pa, and 0.25 Pa, respectively. Among these stations, OHP is approximately 977 km from Stromboli volcano, I26DE is approximately 1125 km from the source, and CEA is approximately 1507 km from the source.

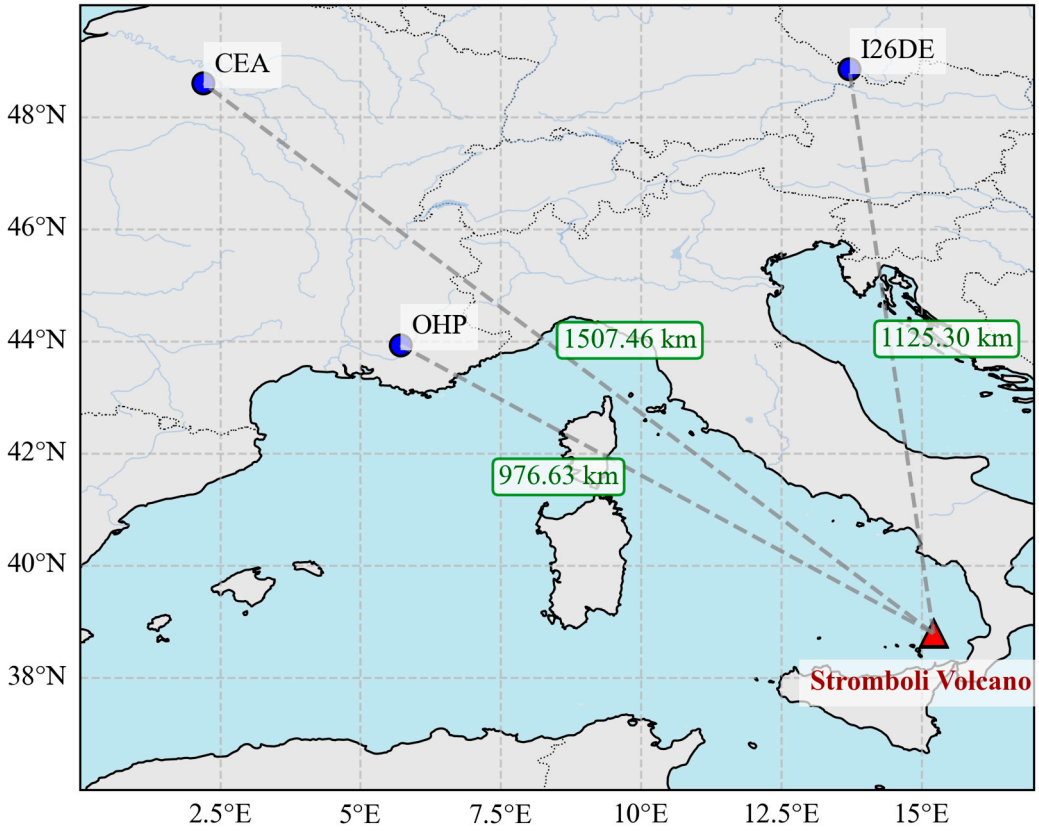


Figure 5. Spatial distribution of CEA, I26DE, and OHP relative to Stromboli volcano.

3.1.3. The 15 January 2022 Hunga Eruption, Tonga

On 15 January 2022, the Hunga Tonga–Hunga Hualapai submarine volcano in the Kingdom of Tonga, South Pacific, erupted violently. A large amount of gas and ash formed a mushroom cloud resembling that of a nuclear explosion, and the eruption column reached a height of at least 25 km. This event was the largest volcanic eruption in more than 30 years. The eruption excited broadband atmospheric waves, including low-frequency Lamb waves, acoustic-gravity waves, and infrasound waves. Its signals were synchronously captured worldwide by ground barometers, infrasound arrays, seismic stations, hydroacoustic stations, satellites, and GNSS systems [36], among which the infrasound observations were particularly prominent. All 53 certified infrasound stations operating in the International Monitoring System (IMS) at that time recorded this event, making it the first global-scale single-event observation case since the operation of the IMS infrasound network [37].

In this study, data recorded by 16 infrasound stations worldwide were obtained using ObsPy [38]. The spatial distribution of these stations is shown in Figure 7. The distances between the stations and the volcanic source ranged from approximately 4800 to 17,000 km, covering long-range to global-scale observation distances. The stations also provided favorable azimuthal coverage, offering comprehensive infrasonic observational constraints. Therefore, this dataset provides a reliable basis for validating and evaluating the proposed method.

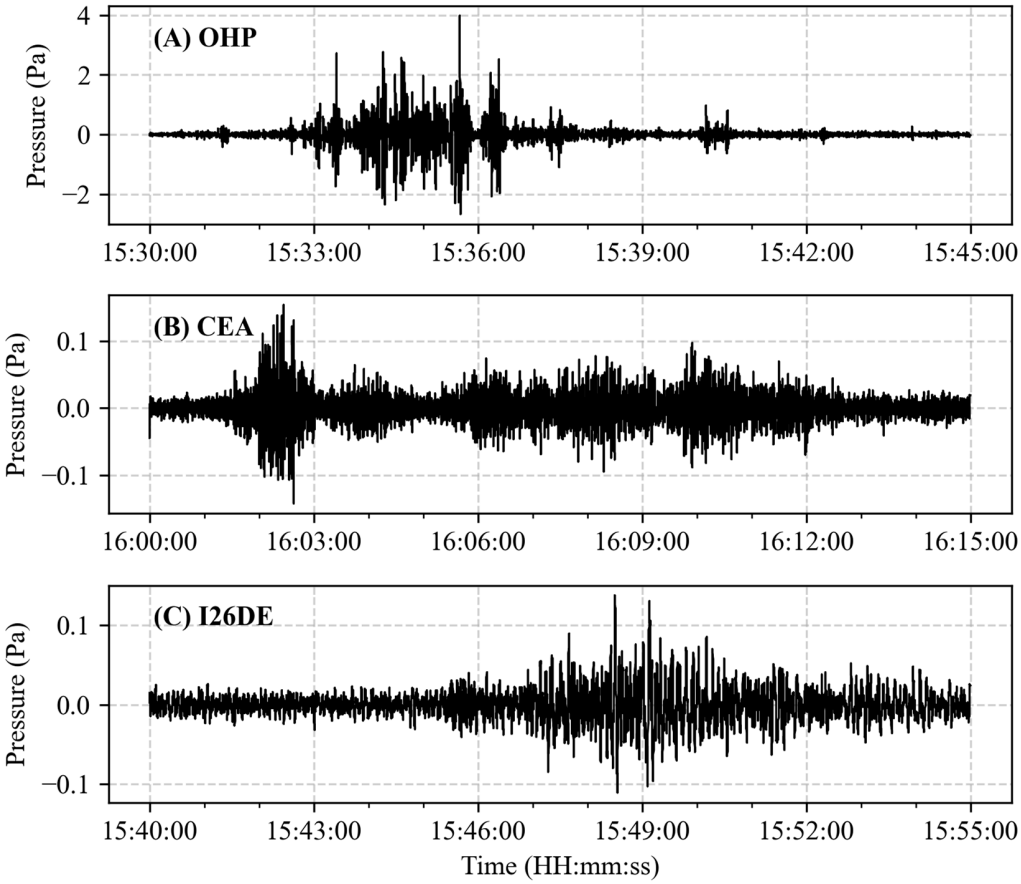


Figure 6. Infrasound signals generated by the Stromboli volcanic eruption on 3 July 2019.

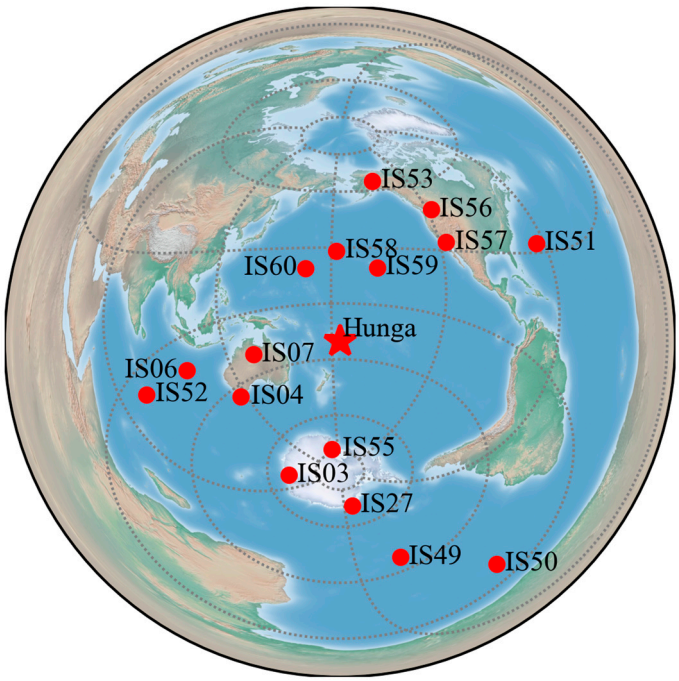


Figure 7. Global distribution of the 16 infrasound stations used for the Hunga eruption case.

3.2. Experimental Results

3.2.1. Ingolstadt Refinery Explosion

The direction of arrival was estimated using the infrasound data recorded by the IGADE and PSZI stations. The results are listed in Table 1. Only two infrasound stations, IGADE and PSZI, were available for localization, resulting in relatively weak observational geometric constraints. The azimuth calculated from the PSZI infrasound data exhibited a large deviation from the theoretical value, with an error of up to 5.09°. Because only two stations provided infrasound data in this case, direct intersection of the two arrival directions produced a single intersection point. The initial event location was therefore estimated as (11.569847° E, 48.263409° N), which is approximately 56.95 km from the true explosion location, as shown in Figure 8.

Table 1. Direction-finding results for the Ingolstadt refinery explosion.

Infrasound Station	Theoretical Value	Measured Value	Error
IGADE	−19.92°	−19.09°	0.83°
PSZI	95.37°	90.29°	−5.09°

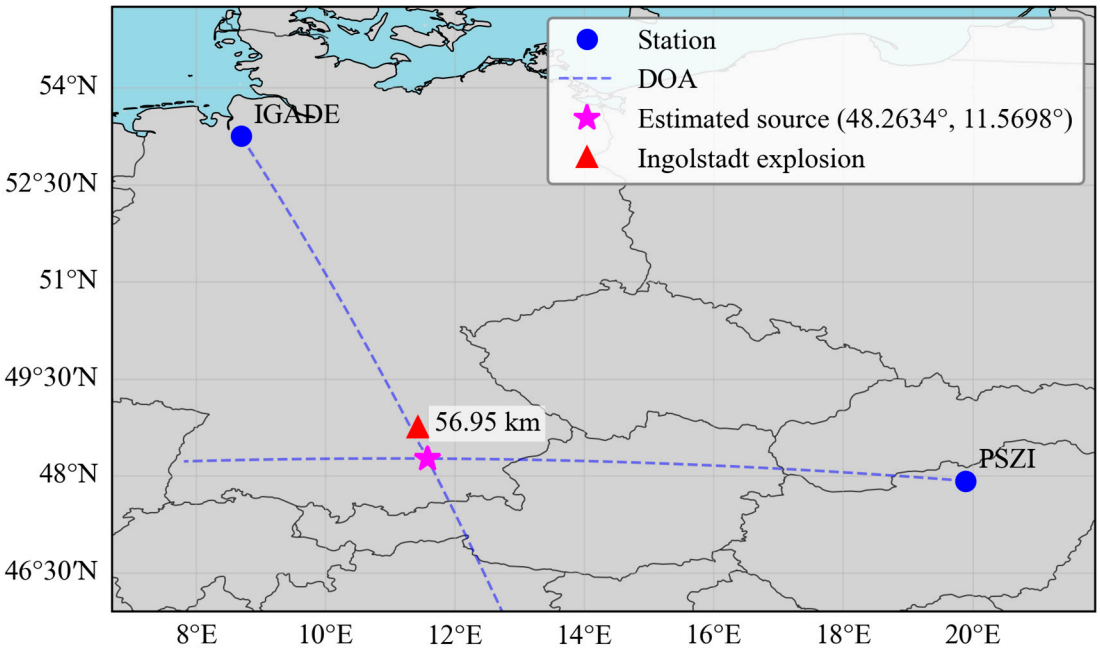


Figure 8. Initial geometric localization result for the Ingolstadt refinery explosion.

Centered on the initial geometric location, a localized candidate search region was established. Combined with the hybrid atmospheric model incorporating ERA5 reanalysis data, eigenray searching and theoretical travel-time computations were conducted for different candidate source locations. To uniformly evaluate the goodness-of-fit of travel times across candidate locations, an objective function for location inversion was constructed based on the root mean square error (RMSE) between theoretical and observed travel times across multiple stations. Table 2 lists the theoretical travel times and RMSE of travel-time residuals for each candidate location under different topographic conditions.

Among all investigated candidate locations, when actual topography was taken into account, the candidate point (48.722868° N, 11.257867° E) achieved the minimum RMSE of travel-time residuals at 238.50 s; the RMSE for the same location without considering topography was 244.07 s. The incorporation of topography reduced the RMSE at this

candidate location by 5.57 s, representing an improvement of approximately 2.28%. The final inverted location was determined to be (48.722868° N, 11.257867° E), yielding a location error of 13.23 km, which corresponds to an error reduction of 76.77%. These results demonstrate that when the station network is sparse and individual station back-azimuth estimates suffer from significant deviations, relying solely on back-azimuth intersection tends to incur substantial errors. In contrast, travel-time constraints provide crucial additional corrections to the location results, effectively enhancing the positioning reliability under few-station conditions.

Table 2. Theoretical travel times and RMSE of travel-time residuals under the hybrid atmospheric model for the Ingolstadt refinery explosion.

Candidate Source Location (°N, °E)	Topography Considered	IGADE (s)	PSZI (s)	RMSE (s)
[48.722868, 11.257867]	No	1663.76	2737.77	244.07
	Yes	1674.39	2734.92	238.50
[48.722868, 11.757867]	No	2427.72	2651.04	438.70
	Yes	2429.50	2651.87	440.08
[48.222868, 11.257867]	No	2539.81	2733.62	533.71
	Yes	2504.94	2729.44	509.86
[48.222868, 11.757867]	No	2539.81	1850.83	646.45
	Yes	2504.94	1828.24	638.63
[48.222868, 12.257867]	No	2583.49	1792.53	696.78
	Yes	2572.27	1778.32	697.57
Observed Travel Time (s)		1843.25	2442.95	

3.2.2. Localization Validation for the Stromboli Volcanic Eruption

The direction of arrival of the Stromboli volcanic infrasound signals was calculated using the method described in Section 2.2.1. The results are shown in Table 3. The three far-field stations, OHP, IS26, and CEA, provided richer azimuthal observation information; however, the azimuth errors differed significantly among the stations. The azimuth of the infrasonic signal arriving at OHP differed from the theoretical value by 0.11°, which was the smallest error. In contrast, the azimuth of the infrasonic signal arriving at CEA differed from the theoretical value by 3.68°, which was the largest error.

Table 3. Direction-finding results for the Stromboli volcanic eruption.

Infrasound Station	Theoretical Value	Measured Value	Error
OHP	122.56°	122.67°	0.11°
IS26	173.33°	174.59°	1.26°
CEA	131.51°	135.19°	3.68°

Using the arrival directions listed in Table 3 for intersection localization, three intersection points were obtained, and least-squares optimization was applied, as shown in Figure 9. The initial localization result differed from the true volcanic location by approximately 35.58 km. This indicates that multi-station observations can improve the stability of preliminary localization to some extent, but they still cannot completely eliminate the influence of atmospheric propagation effects on azimuth estimation.

Furthermore, the physical forward model and propagation travel-time information were incorporated to perform joint inversion. Table 4 presents the theoretical travel times and the corresponding travel-time residuals at each station for 12 candidate source locations

under the hybrid atmospheric model. Under the flat-surface assumption, the candidate location (38.789727° N, 15.144599° E) yielded the minimum multi-station joint travel-time residual of 438.75 s. The final location error was 5.93 km, representing an 83.33% improvement in positioning accuracy compared with conventional localization methods. This result indicates that, for long-range volcanic infrasound events, an increased number of recording stations enhances geometric constraints, while ray-tracing travel-time optimization further compensates for errors induced by ray-path curvature and effective sound-speed variations. The combination of both mechanisms substantially improves localization accuracy.

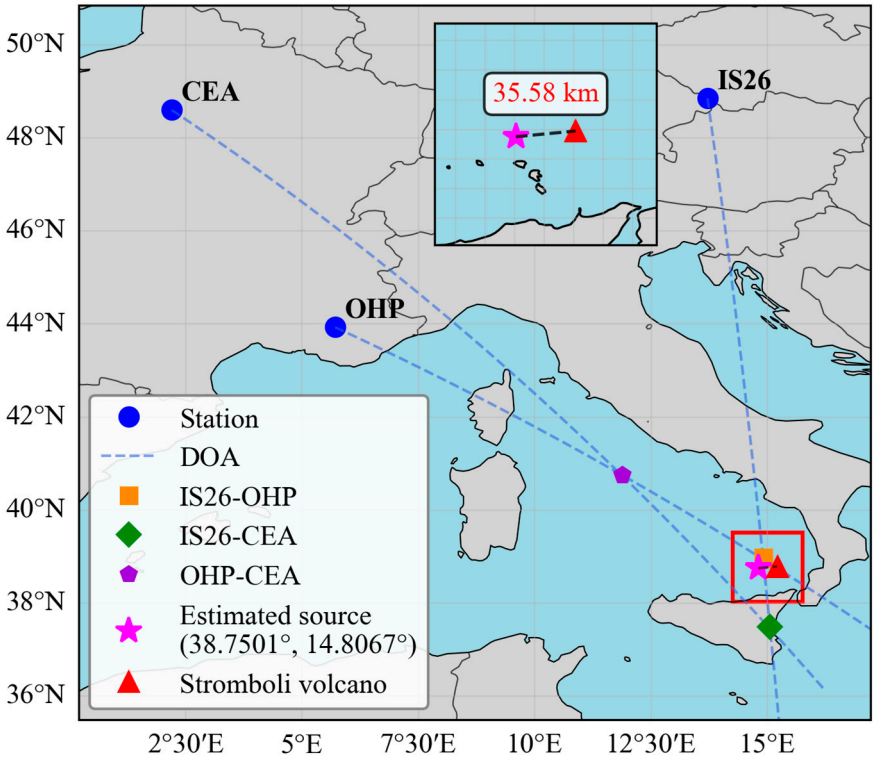


Figure 9. Initial geometric localization result for the Stromboli eruption.

Table 4. Theoretical travel times and RMSE of travel-time residuals under the hybrid atmospheric model for the Stromboli volcanic eruption.

Candidate Source Location (°N, °E)	Topography	CEA (s)	IS26 (s)	OHP (s)	RMSE (s)
[38.789727, 14.744599]	No	5637.17	4311.03	3161.84	679.98
	Yes	5609.89	4334.56	3364.93	698.91
[38.789727, 14.944599]	No	5660.50	4324.85	3210.96	699.88
	Yes	5663.57	4331.67	3446.75	739.29
[38.789727, 15.144599]	No	5031.99	4346.36	3244.36	438.75
	Yes	5646.17	4290.52	3474.69	726.70
[38.789727, 14.544599]	No	5186.35	4303.84	3330.81	495.26
	Yes	5642.22	4361.31	2970.31	690.07
[38.589727, 14.544599]	No	5660.66	4367.42	3176.59	708.43
	Yes	5662.31	4439.92	3382.07	756.50
[38.589727, 14.744599]	No	5680.05	4370.17	3219.18	722.79
	Yes	5664.81	4384.38	3418.40	748.30

Table 4. *Cont.*

Candidate Source Location (°N, °E)	Topography	CEA (s)	IS26 (s)	OHP (s)	RMSE (s)
[38.589727, 14.944599]	No	5029.86	4380.96	3245.61	453.70
	Yes	5110.50	4458.24	3502.63	573.47
[38.589727, 15.144599]	No	5744.51	4390.66	3279.58	767.13
	Yes	5178.88	4408.95	3547.57	589.40
[38.989727, 14.544599]	No	5572.01	4188.05	3302.89	633.64
	Yes	5528.30	4231.71	3293.03	620.36
[38.989727, 14.744599]	No	5165.62	4262.80	3303.57	466.37
	Yes	5647.06	4246.04	3268.17	680.05
[38.989727, 14.944599]	No	5608.29	4190.63	3143.07	634.10
	Yes	5043.76	4243.05	3429.10	448.71
[38.989727, 15.144599]	No	5663.12	4283.75	3216.27	691.20
	Yes	5278.92	4264.64	3417.74	540.68
Observed Travel Time (s)		4605	3768	2998	

3.2.3. Localization of the Hunga Volcanic Eruption

In this section, the previously obtained initial location estimate of the event [35] is used as the reference, and the initial localization procedure is not repeated. In the Hunga volcanic eruption case, the propagation scale reached a global range, and 16 infrasound stations recorded signals from different azimuths. Table 5 presents the back-azimuth calculation results for each station, yielding a final initial location of (19.619728° S, 175.383941° W). Compared with the previous two cases, this scenario involved more complex atmospheric propagation paths and longer propagation distances, placing greater demands on the modeling of Earth curvature, atmospheric waveguides, and wind-field structures.

Table 5. Direction-finding results for the Hunga volcanic eruption event.

Infrasound Station	Theoretical (°)	Measured (°)	Error (°)
IS03	56.303	59.325	−3.022
IS04	96.610	96.222	0.388
IS06	109.884	105.205	4.6798
IS07	100.099	100.281	−0.182
IS27	−167.030	−170.837	3.807
IS49	−160.645	−153.273	−7.372
IS50	−145.988	−140.370	−5.618
IS51	−98.060	−93.034	−5.026
IS52	114.970	113.780	0.89
IS53	−155.185	−154.202	−0.983
IS55	20.025	21.300	−1.275
IS56	−127.654	−140.125	12.471
IS57	−125.375	−133.401	8.026
IS58	176.273	174.903	1.37
IS59	−154.542	−150.220	−4.322
IS60	153.834	152.880	0.954

Local grid-search travel-time optimization was performed under the hybrid atmospheric model. The observed travel times across the 16 stations are listed in Table 6. Table 7 presents the theoretical travel times and the corresponding RMSE of travel-time residuals from four candidate source locations to the 16 infrasound stations. Among them, the candidate location (−20.520629° N, −175.340370° E) achieved the minimum RMSE of 4969.26 s,

which is markedly lower than those of the other three candidate locations. The final localization deviation of the proposed method reached 6.98 km, as shown in Figure 10. Meanwhile, the globally distributed stations provided favorable surrounding observational constraints, which helped reduce the influence of single-path atmospheric model errors or individual station observation errors on the final result. This highlights the importance of multi-station fusion in global infrasound localization.

Table 6. Observed travel times for the Hunga volcanic eruption.

Station	Observed Travel Time (s)	Station	Observed Travel Time (s)
IS03	29,617	IS52	40,664
IS04	24,177	IS53	35,135
IS06	32,181	IS55	22,808
IS07	18,600	IS56	34,145
IS27	33,704	IS57	30,848
IS49	43,362	IS58	19,311
IS50	65,890	IS59	17,998
IS51	38,614	IS60	17,206

Table 7. Theoretical travel times and RMSE of travel-time residuals (s) under the hybrid atmospheric model for the Hunga volcanic eruption.

Candidate Source Location (°N, °E)	[−19.619728, −175.383941]	[−20.520629, −175.340370]	[−19.520629, −176.340370]	[−19.520629, −175.340370]
IS03	29,249.50	28,876.16	28,277.48	29,272.63
IS04	24,142.84	24,144.29	23,745.62	24,170.26
IS06	33,010.61	32,464.58	31,878.85	32,794.80
IS07	18,251.11	17,964.96	18,178.26	18,778.47
IS27	30,856.16	28,584.68	32,420.34	30,703.11
IS49	39,452.18	40,625.49	54,088.34	52,785.43
IS50	59,348.54	61,223.15	70,577.14	69,004.57
IS51	34,286.60	37,684.25	55,173.06	68,547.63
IS52	40,824.70	39,577.49	41,660.79	42,035.86
IS53	21,155.13	21,200.60	19,802.74	19,893.29
IS55	14,533.01	16,074.08	16,046.98	14,602.95
IS56	34,331.58	35,105.01	35,381.32	35,236.56
IS57	28,897.70	29,254.98	29,698.21	28,810.50
IS58	11,476.68	12,732.69	11,371.75	11,456.46
IS59	18,192.22	18,048.62	20,591.28	19,198.14
IS60	10,139.87	10,114.24	10,140.21	10,165.06
RMSE	5390.86	4969.26	7156.46	9432.73

The localization results of the three representative events (see Table 8) show that the proposed two-step infrasound localization method exhibits good adaptability and stability under different station numbers, propagation distances, and observational geometries. Compared with the conventional geometric localization method that relies only on array back-azimuth intersections, the advantages of the proposed method are mainly reflected in two aspects. First, geometric preliminary localization is used to rapidly narrow the search range, avoiding high-cost propagation forward modeling over a global-scale domain. Second, spherical-coordinate ray tracing and travel-time residual optimization are introduced within a local region, allowing the final localization result to be constrained by the actual atmospheric propagation process and thereby reducing systematic biases caused by wind fields, temperature gradients, and Earth curvature.

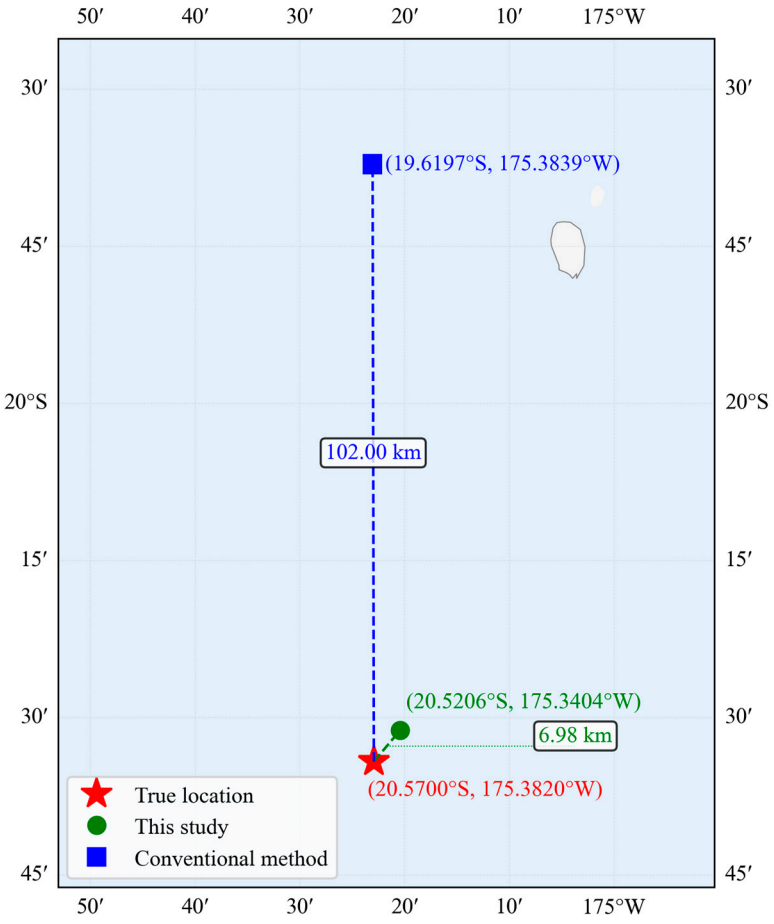


Figure 10. Hunga eruption localization results from the conventional geometric method and the proposed method.

Table 8. Summary of localization performance for the three validation events.

Event	Monitoring Scenario	Geometric Error (km)	Proposed Final Error (km)	Improvement (%)
Ingolstadt refinery explosion	Two-station regional monitoring	56.95	13.23	76.77
Stromboli eruption	Three-station long-range monitoring	35.58	5.93	83.33
Hunga eruption	Global multi-station monitoring	102.00	6.98	93.16

Overall, the three cases show that the localization accuracy of the proposed method does not depend solely on the number of stations. Instead, it is jointly determined by station geometry, azimuth-estimation accuracy, travel-time extraction accuracy, and atmospheric-model accuracy. Under sparse-station conditions, ray-tracing-based travel-time constraints can substantially compensate for insufficient geometric constraints. Under multi-station conditions, fusion of observational information can further improve result stability. Under global-scale conditions, the spherical-coordinate model and geometric correction terms are particularly important for maintaining the physical consistency of propagation modeling.

3.3. Discussion

The proposed two-step framework achieves satisfactory localization accuracy across regional, long-range, and global scales. However, the precision of the estimated source loca-

tion is inherently influenced by several physical and numerical factors, primarily involving arrival-time picking, atmospheric representation, and spatial grid discretization.

In this study, the observed arrival times are determined through a combined pipeline of adaptive threshold detection and Akaike information criterion (AIC) autoregressive refinement. The AIC objective function identifies the physical onset by locating the global minimum of the information-theoretic criterion, effectively avoiding the subjectivity associated with manual picking or simple amplitude peak tracking. Given the high signal-to-noise ratio of the selected event signals, the timing discrepancy between the statistical transition point and the true acoustic onset is strictly confined to a very short time window, rendering its contribution secondary compared to path-integrated propagation deviations.

Infrasonic ray paths are highly sensitive to spatiotemporal gradients in ambient temperature and horizontal winds. Although hybrid atmospheric products (combining ERA5 reanalysis and empirical climatologies such as HWM14/NRLMSIS 2.0) provide realistic background fields, they cannot fully resolve transient mesoscale dynamics, including uncaptured gravity waves and local wind shears. The cumulative effect of these unmodeled high-altitude perturbations over hundreds to thousands of kilometers can lead to ray-path refraction and travel-time shifts, representing the dominant physical source of localization uncertainty.

The current framework minimizes the travel-time residual over discrete candidate grids, which inherently imposes a geometric bound on spatial resolution governed by the chosen grid interval. Nevertheless, because ground-truth locations are documented for all three validation events, the final absolute errors (13.23 km for Ingolstadt, 5.93 km for Stromboli, and 6.98 km for Hunga) empirically demonstrate that the optimized grid solutions lie well within a narrow confidence region consistent with expected atmospheric fluctuations. Future work will investigate probabilistic inversion strategies (e.g., Bayesian formulation or ensemble Monte Carlo modeling) to quantify continuous posterior confidence intervals.

4. Conclusions

This study focuses on the problem of high-accuracy localization of medium-range, long-range, and global-scale infrasonic events and proposes a two-step localization method that integrates spherical-coordinate ray tracing with local travel-time residual optimization. The method first obtains an initial source location through multi-station azimuth intersection, k-means clustering, and least-squares estimation. A local search grid is then constructed around the initial location. Ray tracing in an inhomogeneous moving atmospheric medium is used to calculate the theoretical travel times from candidate source points to each station, and the final location is determined by minimizing the weighted travel-time residuals. While retaining the computational efficiency of conventional geometric localization, this framework introduces physical constraints from atmospheric propagation, thereby balancing computational efficiency and localization accuracy.

The main conclusions of this study are as follows:

In terms of localization methodology, this study constructs a two-stage localization framework consisting of geometric preliminary localization and local grid search. In the preliminary localization stage, array-based direction-finding intersections are used to rapidly determine the candidate region, and clustering-based screening is applied to reduce the influence of abnormal intersection points. In the refined localization stage, the initial-position bias is corrected by matching residuals between ray-tracing-based forward-modeled travel times and observed travel times. This strategy avoids the high computational cost of conventional global grid search while improving the adaptability of localization results to atmospheric propagation effects.

In terms of experimental validation, three representative events were selected: the Ingolstadt refinery explosion, the Stromboli volcanic eruption, and the Hunga volcanic eruption. These events represent sparse-station medium-to-long-range monitoring, multi-station long-range monitoring, and global-scale observation scenarios, respectively. The experimental results show that the final localization errors of the proposed method in the three cases were 13.23 km, 5.93 km, and 6.98 km, respectively. Compared with conventional geometric localization methods, the localization accuracy was improved by more than 76% in all cases, demonstrating the effectiveness, stability, and generalization capability of the proposed method across different propagation scales and network configurations.

The experimental results further indicate that atmospheric propagation modeling is a key factor in improving long-range infrasound localization accuracy. Conventional geometric localization is mainly controlled by azimuth error. When the propagation distance increases or the number of stations is small, localization errors can accumulate rapidly. By introducing theoretical travel-time constraints, the proposed method can effectively correct systematic biases caused by wind fields, temperature gradients, and propagation-path bending. The fusion of multi-station observational information can further strengthen geometric constraints and reduce the influence of single-station errors on the final result.

In summary, the proposed method provides a reliable and engineering-applicable technical solution for rapid and high-accuracy localization of infrasonic events. It can serve applications such as nuclear-test monitoring, major explosion identification, volcanic-eruption warning, and global atmospheric acoustic-event monitoring. Future research can be improved in three aspects: first, by introducing real-time three-dimensional atmospheric assimilation data with higher spatiotemporal resolution to improve the accuracy of propagation-environment representation; second, by quantifying localization uncertainty and providing confidence regions for source locations; and third, by optimizing ray-tracing and grid-search strategies to further improve computational efficiency and real-time applicability for global-scale events.

Author Contributions: Conceptualization, H.Y. and X.P.; methodology, H.Y.; software, H.Y. and F.Y.; validation, H.Y., F.Y. and X.P.; formal analysis, H.Y.; investigation, H.Y.; resources, H.Y.; data curation, H.Y.; writing—original draft preparation, H.Y.; writing—review and editing, H.Y. and F.Y.; visualization, H.Y.; supervision, X.P. All authors have read and agreed to the published version of the manuscript.

Funding: This research received no external funding.

Data Availability Statement: The data and code that support the findings of this study are openly available from the corresponding author upon reasonable request.

Conflicts of Interest: The authors declare no conflicts of interest.

References

1. Roth, P.R. Effective Measurements Using Digital Signal Analysis. *IEEE Spectr.* **1971**, *8*, 62–70. [CrossRef]
2. Carter, G.C.; Nuttall, A.H.; Cable, P.G. The Smoothed Coherence Transform. *Proc. IEEE* **1973**, *61*, 1497–1498. [CrossRef]
3. Scarbrough, K.; Ahmed, N.; Carter, G. *An Experimental Comparison of the Cross Correlation and SCOT Techniques for Time Delay Estimation*; Institute of Electrical and Electronics Engineers: Denver, CO, USA, 1980; Volume 5, pp. 807–810.
4. Scarbrough, K.; Ahmed, N.; Youn, D.; Carter, G. *On the Scot and Roth Algorithms for Time Delay Estimation*; Institute of Electrical and Electronics Engineers: Paris, France, 1982; Volume 7, pp. 371–374.
5. Meng, L.; Li, X.-H.; Zhang, W.-G.; Dai-Zhi, L. The Generalized Cross-Correlation Method for Time Delay Estimation of Infrasound Signal. In *Proceedings of the 2015 Fifth International Conference on Instrumentation and Measurement, Computer, Communication and Control (IMCCC), Qinhuangdao, China, 18–20 September 2015*; IEEE: Piscataway, NJ, USA, 2015; pp. 1320–1323.
6. Jordan, T.H.; Keith, A. Sverdrup Teleseismic Location Techniques and Their Application to Earthquake Clusters in the South-Central Pacific. *Bull. Seismol. Soc. Am.* **1981**, *71*, 1105–1130. [CrossRef]

7. Shang, C.; Teng, P.; Lyu, J.; Yang, J.; Cheng, W. Localization algorithm for infrasound source in air and its error analysis. *Tech. Acoust.* **2020**, *39*, 360–365. [CrossRef]
8. Pilger, C.; Gaebler, P.; Hupe, P.; Ott, T.; Drolshagen, E. Global Monitoring and Characterization of Infrasound Signatures by Large Fireballs. *Atmosphere* **2020**, *11*, 83. [CrossRef]
9. Brown, P.G.; Whitaker, R.W.; ReVelle, D.O.; Tagliaferri, E. Multi-Station Infrasonic Observations of Two Large Bolides: Signal Interpretation and Implications for Monitoring of Atmospheric Explosions. *Geophys. Res. Lett.* **2002**, *29*, 14-1–14-4. [CrossRef]
10. Herrin, E.; Golden, P.; Negraru, P.; Andre, W.; Bass, H.; Garces, M.; Hedlin, M.; McKenna, M.; Norris, D.; Osborne, D.; et al. Infrasound Calibration Explosions from Rockets Launched at White Sands Missile Range. In Proceedings of the 28th Seismic Research Review: Ground: Based Nuclear Explosion Monitoring Technologies, Orlando, FL, USA, 19–21 September 2006; pp. 910–918.
11. Sahetapy-Engel, S.T.; Harris, A.J.L.; Marchetti, E. Thermal, Seismic and Infrasound Observations of Persistent Explosive Activity and Conduit Dynamics at Santiaguito Lava Dome, Guatemala. *J. Volcanol. Geotherm. Res.* **2008**, *173*, 1–14. [CrossRef]
12. Lü, J.; Yang, Y.; Guo, Q.; Feng, H.; Teng, P. Anomalous infrasonic waves before an small earthquake in Beijing. *Chin. J. Geophys.* **2012**, *55*, 3379–3385. (In Chinese) [CrossRef]
13. Yang, Y.-C.; Guo, Q.; Lü, J.; Teng, P.-X. Observation and study of precursor infrasound waves emitted before several strong earthquakes. *Acta Phys. Sin.* **2014**, *63*, 224–237. [CrossRef]
14. Gal, M.; Reading, A.M.; Ellingsen, S.P.; Koper, K.D.; Burlacu, R.; Gibbons, S.J. Deconvolution Enhanced Direction of Arrival Estimation Using One- and Three-Component Seismic Arrays Applied to Ocean Induced Microseisms. *Geophys. J. Int.* **2016**, *206*, 345–359. [CrossRef]
15. den Ouden, O.F.C.; Assink, J.D.; Smets, P.S.M.; Shani-Kadmiel, S.; Averbuch, G.; Evers, L.G. CLEAN Beamforming for the Enhanced Detection of Multiple Infrasonic Sources. *Geophys. J. Int.* **2020**, *221*, 305–317. [CrossRef]
16. Anderson, J.F.; Johnson, J.B.; Mikesell, T.D.; Liberty, L.M. Remotely Imaging Seismic Ground Shaking via Large-N Infrasound Beamforming. *Commun. Earth Environ.* **2023**, *4*, 399–410. [CrossRef]
17. Ma, Y.; Zheng, Y.; Fan, J.B.; Li, P. Research on an Infrasound Localization Method Based on Spatial Spectrum Estimation. In *National Security Geophysics Series (IX): Disaster Prevention and Mitigation and National Security*; Xi'an Cartographic Publishing House: Xi'an, China, 2013; pp. 6, 341–346.
18. Meng, L.; Li, X.; Chen, D.; Yang, T. A High-Resolution Method for Estimating the Azimuth of Infrasound Signals. In *Proceedings of the 2016 3rd International Conference on Materials Engineering, Manufacturing Technology and Control, Taiyuan, China, 27–28 April 2016*; Atlantis Press: Paris, France, 2016.
19. Meng, L.; Li, X.H.; Liu, D.Z. Two-Dimensional Subspace Algorithm for the Slowness and Azimuth of Infrasound Signals in the Distant Events Monitoring. *Chin. J. Geophys.* **2017**, *60*, 678–687.
20. Lu, S.K.; Xu, W.; Lin, Y.G.; Chen, X.Z.; Dong, L.; Zhu, B.S.; Tao, L. Infrasound Event Detection Based on a Segmented Progressive MUSIC Algorithm. In *National Security Geophysics Series (XV): Silk Road Environment and Geophysics, Proceedings of the Conference of the National Security Geophysics Committee of the Chinese Geophysical Society and the Military Geophysics Committee of the Shaanxi Geophysical Society, Zhangye, Gansu, China, 2019*; Xi'an Cartographic Publishing House: Xi'an, China, 2019; pp. 100–105.
21. Olivier, d.O.; Jelle, A.; Pieter, S. Laslo Evers Well-Founded Parameters for CLEAN and MUSIC Beamforming. In Proceedings of the EGU General Assembly Conference Abstracts, Vienna, Austria, 8–13 April 2018.
22. De Negri, R.; Matoza, R.S. Rapid Location of Remote Volcanic Infrasound Using 3D Ray Tracing and Empirical Climatologies: Application to the 2011 Cordón Caulle and 2015 Calbuco Eruptions, Chile. *J. Geophys. Res. Solid Earth* **2023**, *128*, e2022JB025735. [CrossRef]
23. De Negri, R.S.; Matoza, R.S.; Hupe, P.; Le Pichon, A.; Rose, K.M.; Cevuard, S.; Niroa, J.J. Evaluating the Temporal Capability of Empirical Climatologies for Rapid Long-Range Volcanic Infrasound Propagation Estimates Using a Multidecadal Data Set of Persistent Vanuatu Volcanic Eruptions. *Geophys. J. Int.* **2025**, *241*, 268–290. [CrossRef]
24. Ceranna, L.; Le Pichon, A.; Green, D.N.; Mialle, P. The Buncefield Explosion: A Benchmark for Infrasound Analysis across Central Europe. *Geophys. J. Int.* **2009**, *177*, 491–508. [CrossRef]
25. Blom, P.S.; Marcillo, O.; Arrowsmith, S.J. Improved Bayesian Infrasonic Source Localization for Regional Infrasound. *Geophys. J. Int.* **2015**, *203*, 1682–1693. [CrossRef]
26. Pilger, C.; Ceranna, L.; Ross, J.O.; Vergoz, J.; Le Pichon, A.; Brachet, N.; Blanc, E.; Kero, J.; Liszka, L.; Gibbons, S.; et al. The European Infrasound Bulletin. *Pure Appl. Geophys.* **2018**, *175*, 3619–3638. [CrossRef]
27. Arrowsmith, S.; Park, J.; Che, I.-Y.; Stump, B.; Averbuch, G. Event Location with Sparse Data: When Probabilistic Global Search Is Important. *Seismol. Res. Lett.* **2020**, *92*, 976–985. [CrossRef]
28. Fee, D.; Toney, L.; Kim, K.; Sanderson, R.W.; Iezzi, A.M.; Matoza, R.S.; De Angelis, S.; Jolly, A.D.; Lyons, J.J.; Haney, M.M. Local Explosion Detection and Infrasound Localization by Reverse Time Migration Using 3-D Finite-Difference Wave Propagation. *Front. Earth Sci.* **2021**, *9*, 620813. [CrossRef]

29. Modrak, R.T.; Arrowsmith, S.J.; Anderson, D.N. A Bayesian Framework for Infrasound Location. *Geophys. J. Int.* **2010**, *181*, 399–405. [CrossRef]
30. Marcillo, O.; Arrowsmith, S.; Whitaker, R.; Anderson, D.; Nippress, A.; Green, D.N.; Drob, D. Using Physics-Based Priors in a Bayesian Algorithm to Enhance Infrasound Source Location. *Geophys. J. Int.* **2014**, *196*, 375–385. [CrossRef]
31. Nippress, A.; Green, D.N.; Marcillo, O.E.; Arrowsmith, S.J. Generating Regional Infrasound Celerity-Range Models Using Ground-Truth Information and the Implications for Event Location. *Geophys. J. Int.* **2014**, *197*, 1154–1165. [CrossRef]
32. Blom, P.; Euler, G.; Marcillo, O.; Dannemann Dugick, F. Evaluation of a Pair-Based, Joint-Likelihood Association Approach for Regional Infrasound Event Identification. *Geophys. J. Int.* **2020**, *221*, 1750–1764. [CrossRef]
33. Wang, R.; Yi, X.; Yu, L.; Zhang, C.; Wang, T.; Zhang, X. Infrasound Source Localization of Distributed Stations Using Sparse Bayesian Learning and Bayesian Information Fusion. *Remote Sens.* **2022**, *14*, 3181. [CrossRef]
34. Blom, P.; Waxler, R. Modeling and Observations of an Elevated, Moving Infrasonic Source: Eigenray Methods. *J. Acoust. Soc. Am.* **2017**, *141*, 2681–2692. [CrossRef] [PubMed]
35. Yin, H. Research on Infrasound Localization Method Based on Wide Area Monitoring Network. Master's Thesis, Academy of Military Sciences, Beijing, China, 2022.
36. Matoza, R.S.; Fee, D.; Assink, J.D.; Iezzi, A.M.; Green, D.N.; Kim, K.; Toney, L.; Lecocq, T.; Krishnamoorthy, S.; Lalande, J.-M.; et al. Atmospheric Waves and Global Seismoacoustic Observations of the January 2022 Hunga Eruption, Tonga. *Science* **2022**, *377*, 95–100. [CrossRef] [PubMed]
37. Vergoz, J.; Hupe, P.; Listowski, C.; Le Pichon, A.; Garcés, M.A.; Marchetti, E.; Labazuy, P.; Ceranna, L.; Pilger, C.; Gaebler, P.; et al. IMS Observations of Infrasound and Acoustic-Gravity Waves Produced by the January 2022 Volcanic Eruption of Hunga, Tonga: A Global Analysis. *Earth Planet. Sci. Lett.* **2022**, *591*, 117639. [CrossRef]
38. Krischer, L.; Megies, T.; Barsch, R.; Beyreuther, M.; Lecocq, T.; Caudron, C.; Wassermann, J. ObsPy: A Bridge for Seismology into the Scientific Python Ecosystem. *Comput. Sci. Disc.* **2015**, *8*, 014003. [CrossRef]

Disclaimer/Publisher's Note: The statements, opinions and data contained in all publications are solely those of the individual author(s) and contributor(s) and not of MDPI and/or the editor(s). MDPI and/or the editor(s) disclaim responsibility for any injury to people or property resulting from any ideas, methods, instructions or products referred to in the content.